APL Materials

RESEARCH ARTICLE | AUGUST 15 2024

# Surface reconstructions and electronic structure of metallic delafossite thin films

Qi Song ; Zhiren He ; Brendan D. Faeth ; Christopher T. Parzyck ; Anna Scheid ; Chad J. Mowers ; Yufan Feng ; Qing Xu ; Sonia Hasko ; Jisung Park ; Matthew R. Barone ; Y. Eren Suyolcu ; Peter A. van Aken ; Betül Pamuk ; Craig J. Fennie; Phil D. C. King ; Kyle M. Shen ; Darrell G. Schlom



*APL Mater.* 12, 081117 (2024)
https://doi.org/10.1063/5.0217540

APL Materials ARTICLE pubs.aip.org/aip/apm

# Surface reconstructions and electronic structure of metallic delafossite thin films

Cite as: APL Mater. 12, 081117 (2024); doi: 10.1063/5.0217540
Submitted: 5 May 2024 • Accepted: 22 July 2024 •
Published Online: 15 August 2024

View Online Export Citation CrossMark

Qi Song,[1,a] Zhiren He,[2] Brendan D. Faeth,[3] Christopher T. Parzyck,[4] Anna Scheid,[5] Chad J. Mowers,[4] Yufan Feng,[3,6] Qing Xu,[3] Sonia Hasko,[3] Jisung Park,[1] Matthew R. Barone,[3] Y. Eren Suyolcu,[5] Peter A. van Aken,[5] Betül Pamuk,[3,7] Craig J. Fennie,[2] Phil D. C. King,[8] Kyle M. Shen,[4,9] and Darrell G. Schlom[1,9,10,a]

## AFFILIATIONS

[1]Department of Materials Sciences and Engineering, Cornell University, Ithaca, New York 14853, USA
[2]Department of Applied and Engineering Physics, Cornell University, Ithaca, New York 14853, USA
[3]Platform for the Accelerated Realization, Analysis, and Discovery of Interface Materials (PARADIM), Cornell University, Ithaca, New York 14853, USA
[4]Department of Physics, Laboratory of Atomic and Solid State Physics, Cornell University, Ithaca, New York 14853, USA
[5]Max Planck Institute for Solid State Research, Heisenbergstrasse 1, Stuttgart 70569, Germany
[6]Robert Frederick Smith School of Chemical and Biomolecular Engineering, Cornell University, Ithaca, New York 14853, USA
[7]Department of Physics, Williams College, Williamstown, Massachusetts 01267, USA
[8]SUPA, School of Physics and Astronomy, University of St Andrews, St Andrews KY16 9SS, United Kingdom
[9]Kavli Institute at Cornell for Nanoscale Science, Ithaca, New York 14853, USA
[10]Leibniz-Institut für Kristallzüchtung, Max-Born-Straße 2, 12489 Berlin, Germany

[a]**Authors to whom correspondence should be addressed:** qisong@cornell.edu and schlom@cornell.edu

## ABSTRACT

The growing interest in the growth and study of thin films of low-dimensional metallic delafossites, with the general formula $ABO_2$, is driven by their potential to exhibit electronic and magnetic characteristics that are not accessible in bulk systems. The layered structure of these compounds introduces unique surface states as well as electronic and structural reconstructions, making the investigation of their surface behavior pivotal to understanding their intrinsic electronic structure. In this work, we study the surface phenomena of epitaxially grown $PtCoO_2$, $PdCoO_2$, and $PdCrO_2$ films, utilizing a combination of molecular-beam epitaxy and angle-resolved photoemission spectroscopy. Through precise control of surface termination and treatment, we discover a pronounced $\sqrt{3} \times \sqrt{3}$ surface reconstruction in $PtCoO_2$ films and $PdCoO_2$ films, alongside a $2 \times 2$ surface reconstruction observed in $PdCrO_2$ films. These reconstructions have not been reported in prior studies of delafossites. Furthermore, our computational investigations demonstrate the $BO_2$ surface's relative stability compared to the $A$-terminated surface and the significant reduction in surface energy facilitated by the reconstruction of the $A$-terminated surface. These experimental and theoretical insights illuminate the complex surface dynamics in metallic delafossites, paving the way for future explorations of their distinctive properties in low-dimensional studies.



In recent years, metallic oxides with a delafossite structure have captured significant attention due to their extraordinary structural and electronic characteristics. $PtCoO_2$ single crystals are distinguished by their unparalleled high conductivity per carrier. Similarly, $PdCoO_2$ single crystals possess the longest mean free path of up to 20 $\mu$m at 4 K, surpassing all other known oxide materials.[1–3] The structure of these delafossites consists of layers of platinum (or palladium) that create a single, closed electron pocket at the center of the Brillouin zone at the Fermi level ($E_F$), which is pivotal for the high conductivity in $PtCoO_2$ ($PdCoO_2$) single crystals.[4–6]

The $CoO_2$ layers adjacent to these conductive platinum (or palladium) layers serve as insulating spacers, leading to the out-of-plane resistivity being more than 1000 times higher than the in-plane resistivity in $PdCoO_2$ single crystals at low temperature.[1,7] Notably, $PtCoO_2$ films maintain relatively high conductivity even with reduced dimensionality, exhibiting diminished sensitivity to film thickness in comparison to copper.[8] Among delafossite compounds, $PdCrO_2$ is particularly remarkable for its unique combination of

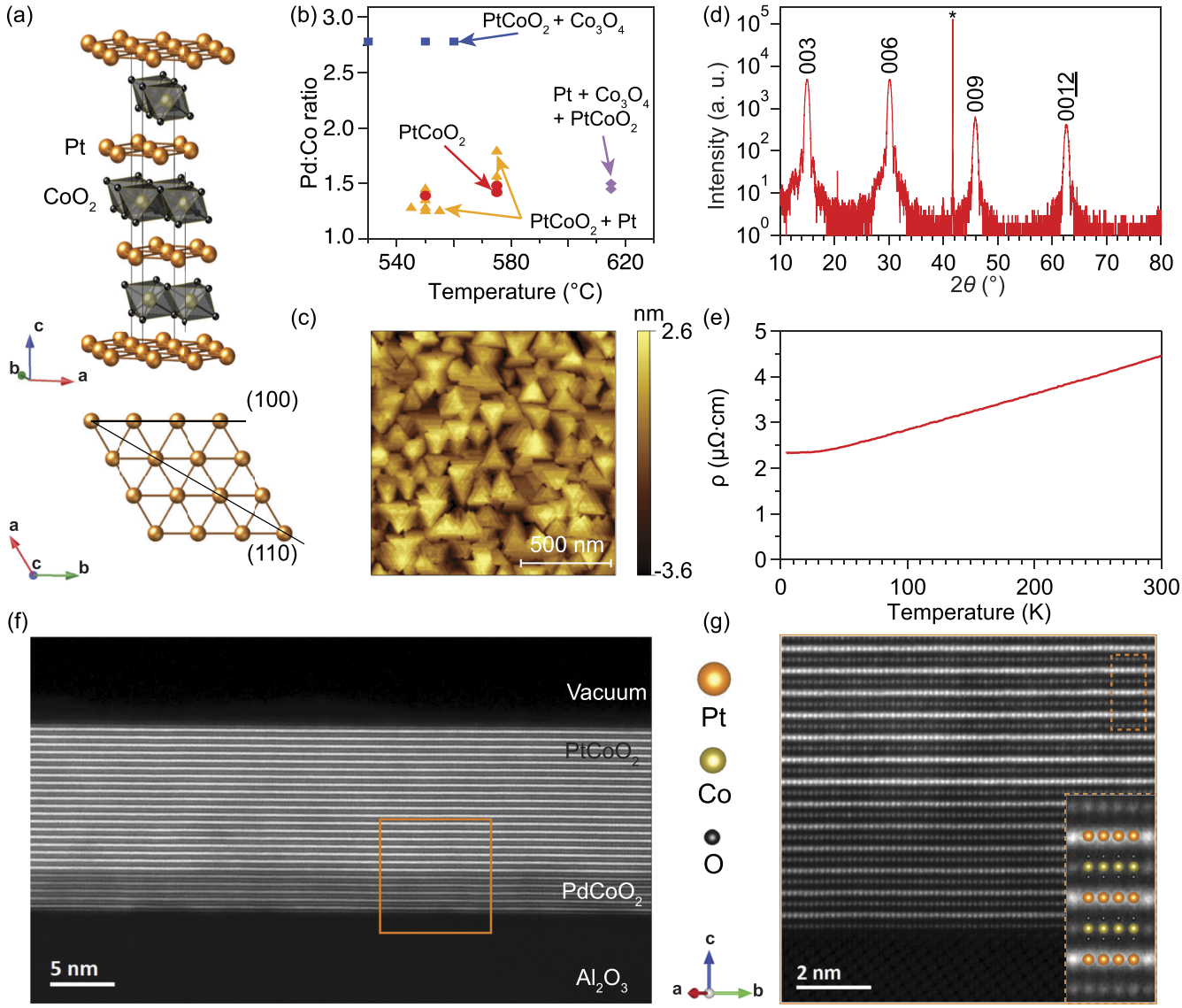


**FIG. 1.** Structural and electrical characterizations of $PtCoO_2$ thin films grown on (001) $Al_2O_3$ substrates by MBE. (a) Crystal structure of $PtCoO_2$, with (100) and (110) planes illustrated on the atomic (001) plane by the black lines. (b) Diagram showing the phases obtained as a function of substrate temperature and Pt:Co ratios during film growth by co-deposition on (001) $Al_2O_3$ substrates. Red circles indicate phase-pure $PtCoO_2$ films, blue squares indicate $PtCoO_2$ films in which $Co_3O_4$ exists as a second phase, yellow triangles indicate conditions under which platinum exists as a second phase, and purple diamonds indicate where $Co_3O_4$ and platinum impurity phases also exist in the $PtCoO_2$ films. All $PtCoO_2$ films described here are deposited onto 4-nm-thick $PdCoO_2$ films. (c) Atomic force microscopy image of a 13.3-nm-thick $PtCoO_2$ film deposited on top of a 4.0-nm-thick $PdCoO_2$ buffer layer. (d) X-ray diffraction of the same $PtCoO_2$ thin film characterized in (c). * denotes the 006 peak of the (001) $Al_2O_3$ substrate. (e) Temperature-dependent resistivity measurements of the same $PtCoO_2$ film characterized in (c). (f) STEM-HAADF image of a $PtCoO_2$ film grown on a 4-nm-thick buffer layer of $PdCoO_2$ grown on a (001) $Al_2O_3$ substrate, viewed along the [201] zone axis of $PtCoO_2$. The film shows high crystalline quality with abrupt interfaces. (g) A higher magnification view of the region outlined by the orange box in (f). The inset of (g) displays an overlay with the structural model where platinum gives the strongest contrast, followed by cobalt due to its lower atomic number, whereas oxygen is invisible in the STEM-HAADF image.

antiferromagnetic order (AFM) at around 37 K while maintaining its metallic conductivity.[9,10] It exhibits a finite interlayer coupling between palladium layers and adjacent insulating $CrO_2$ layers, making this an interesting system to study Kondo-like couplings in a hidden Mott material.[9–13]

With their unique layered structures, metallic delafossites offer opportunities to create novel low-dimensional materials with distinctive properties and functionalities. The polar layers in delafossites, denoted as $A^{1+}$ ($A$ = Pt, Pd) and $BO_2^{1-}$ ($B$ = Co, Cr) in the bulk, exhibit distinct surface states when cleaved in vacuum, effectively addressing the challenges posed by polar surfaces.[14] The $A$ polar surfaces facilitate pronounced electron doping and stabilize the surface states of platinum and palladium layers, whereas hole-doped surface states emerge at the $BO_2$ terminations. The $CoO_2$-terminated surface displays a substantial spin splitting of the surface states, arising due to a strong breaking of the inversion-symmetry at the surface.[15] The ferromagnetism observed in the palladium surface state opens up possibilities for creating two-dimensional ferromagnets.[14,16] The superlattice structures of $PdCoO_2$ and $PdCrO_2$, characterized by structural symmetry breaking, provide a potential avenue for studying interlayer electron interactions. In addition, the Fermi surface of $PdCrO_2$, which has predominantly palladium character, undergoes a magnetic reconstruction into a $\sqrt{3} \times \sqrt{3}$ pattern driven by AFM order at low temperatures.[9–13] Despite the significant promise held by low-dimensional delafossites, interpretation of surface reconstruction in thin films is complicated by the simultaneous presence of surface states and electronic reconstructions driven by AFM order. This complexity underscores the need for further detailed investigations to decipher the intricate phenomena underlying these observations.

Through the powerful combination of molecular-beam epitaxy (MBE) and angle-resolved photoemission spectroscopy (ARPES), we have grown films of $PtCoO_2$, $PdCoO_2$, and $PdCrO_2$ with controlled terminations, enabling a detailed investigation into their electronic structures. These delafossites exhibit distinct surface reconstructions, including a new $2 \times 2$ surface reconstruction in $PdCrO_2$ that has never been previously reported for any delafossite material. Utilizing first-principles density functional theory (DFT) calculations, we demonstrate that surface reconstructions induced by excess oxygen significantly reduce the surface energy for $A$ terminations, while $BO_2$ terminations exhibit relative stability compared to $A$ terminations. In order to show a comprehensive comparison of the metallic delafossites – $PtCoO_2$, $PdCoO_2$, and $PdCrO_2$—We present side-by-side ARPES, low-energy electron diffraction (LEED), reflection high-energy electron diffraction (RHEED), and first-principles calculations of these materials in the subsequent figures.

Metallic delafossite thin films of $PtCoO_2$, $PdCoO_2$, and $PdCrO_2$ are synthesized in a Veeco Gen10 MBE system on (001) sapphire substrates. The atomic structure of delafossites, exemplified by $PtCoO_2$, is illustrated in Fig. 1(a). The growth process is described in detail in the supplementary material. Figure 1(b) presents the results of $PtCoO_2$ films' growth in an adsorption-controlled regime, highlighting the narrow growth window for achieving single-phase $PtCoO_2$ films. The atomic force microscopy image in Fig. 1(c) reveals 180° in-plane rotation twins within these films, in agreement with prior reports of the epitaxial growth of $PtCoO_2$, $PdCoO_2$, and $PdCrO_2$ films on (001) $Al_2O_3$ substrates.[17–25] The pure-phase nature of the $PtCoO_2$ films is confirmed by $\theta$–$2\theta$ x-ray diffraction scans in Fig. 1(d). Resistivity vs temperature measurements of a 13.3-nm-thick $PtCoO_2$ film, conducted using a Quantum Design Physical Property Measurement System (PPMS) employing a four-point van der Pauw geometry, are shown in Fig. 1(e). As the 4-nm-thick $PdCoO_2$ buffer layer is quite flat as shown in the supplementary material (Fig. S1), its resistance has been subtracted out of the resistance measurement of the $PtCoO_2$ film (assuming a simple parallel resistance model). The resistivity of the $PtCoO_2$ film is subsequently calculated using the average thickness of the $PtCoO_2$ film. The residual resistivity ratio (RRR = $\rho_{300K}/\rho_{4K}$) of this $PtCoO_2$ film is 1.91 in its as-grown state (i.e., without any *ex situ* post anneal). For comparison, the RRR of a $PtCoO_2$ single crystal is 52.5.[3] The resistivity of our $PtCoO_2$ film shows a similar linear temperature dependence behavior at high temperatures to that observed in the single crystals. The resistivity comparison between the film and the single crystal is shown in the supplementary material (Fig. S1). The microstructure of the $PtCoO_2$ film is investigated by high-angle annular dark-field scanning transmission electron microscopy (HAADF-STEM) images in Fig. 1(f) and electron energy-loss spectroscopy (EELS) maps found in the supplementary material (Fig. S4). Details on the growth method, as well as the structural and electrical characterization of $PdCrO_2$ films, can be found in the supplementary material (Figs. S2 and S3). All $PtCoO_2$ films investigated in this study exhibit a mixed termination of platinum and $CoO_2$, a result of the adsorption-controlled method utilized to produce them.[24] The palladium termination of the $PdCoO_2$ film and the $CrO_2$ termination of the $PdCrO_2$ films were achieved via the shutter-controlled growth method employed for their growths, as described in prior work.[22,24] Note that not all delafossite films with the described terminations exhibit surface reconstructions. For example, no reconstruction features are present in the Pd- and $CoO_2$- terminated $PdCoO_2$ films described in Ref. 24. This points to a multitude of routes to compensate for the polar surface charge in these materials and a delicate balance of energetics. The precise conditions for stabilizing the different reconstructions observed in these delafossite films, thus, require further study.

ARPES measurements were employed to investigate the bulk states and surface reconstructions of metallic delafossite films. ARPES measurements were conducted using lab-based ARPES systems, which consist of a Scienta Omicron VUV 5000 emitting He-I photons at 21.2 eV and He-II photons at 40.8 eV, and a Fermion Instruments BL1200s discharge lamp for neon-I photons at 16.85 eV.[26] The detection of emitted electrons was performed using a VG Scienta R4000 electron analyzer. Prior to ARPES measurements, all films were exposed to air and then underwent re-annealing in ozone at a background partial pressure of $5 \times 10^{-6}$ Torr at 480 °C for 5 min.

In Figs. 2(a), 2(c), and 2(e), we compare the Fermi surfaces of $PtCoO_2$, $PdCoO_2$, and $PdCrO_2$ films, respectively. Specifically, Fig. 2(a) highlights a hexagonal pocket, denoted as the $\alpha$ band. This intense band is centered at the Γ point and represents the platinum-driven band of $PtCoO_2$, consistent with observation from previous studies on $PtCoO_2$ single crystals.[2] Interestingly, in addition to the bulk $\alpha$ band, additional band features labeled as $\alpha'$ bands are observed both at $E_F$ and 150 meV below it, as shown in Figs. 2(a) and 2(b). These $\alpha'$ bands occupy a similar momentum position to those of the reconstructed bands in $PdCrO_2$ at low temperatures.[11,13] While the known additional bands in the $PdCrO_2$ case arise due to

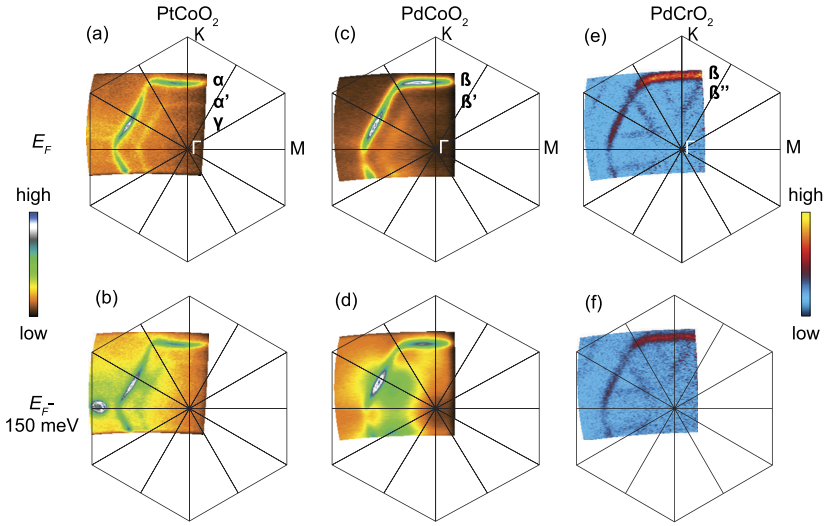


**FIG. 2.** Photoemission intensity maps, collected using 21.2 eV photons, at $E_F$ for (a) the 17.3-nm-thick $PtCoO_2$ film (including 4-nm-thick $PdCoO_2$ buffer layer), (c) a 18.3-nm-thick $PdCoO_2$ film, and (e) a 14.1-nm-thick $PdCrO_2$ film. (b), (d), and (f) represent the same maps as (a), (c), and (e), respectively, but are taken at 150 meV below $E_F$. The data of the $PtCoO_2$ and $PdCoO_2$ films were obtained at a temperature of 6 K, while the $PdCrO_2$ film data were taken at 50 K, i.e., above the AFM transition temperature (37 K) observed in $PdCrO_2$ single crystals. Data of the $PdCrO_2$ film collected at 6 K are shown in Fig. S5 in the supplementary material.

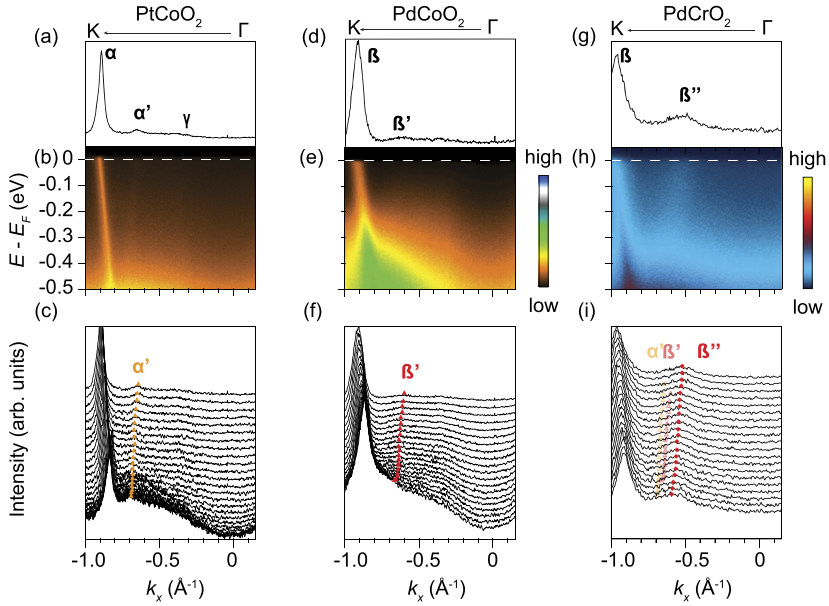


**FIG. 3.** Photoemission intensity distributions of the $PtCoO_2$, $PdCoO_2$, and $PdCrO_2$ films measured at a photon energy of 21.2 eV. (a) Momentum distribution curve across Γ-K of the $PtCoO_2$ film at $E_F$. The platinum bulk state $\alpha$ band, additional $\alpha'$ band, and surface-state-like $\gamma$ band are indicated. (b) The photoemission intensity distribution of the $PtCoO_2$ film between $E_F$ and 500 meV below $E_F$. (c) Momentum distribution curves between $E_F$ and 250 meV below $E_F$ across Γ-K of the $PtCoO_2$ film. The yellow triangles denote the additional $\alpha'$ bands. (d), (e), and (f) The same as (a), (b), and (c), but for the $PdCoO_2$ film. The palladium bulk band in the $PdCoO_2$ film is indicated as the $\beta$ band. An additional $\beta'$ band is also present and is shown by red triangles in (f). It is located at the same momentum position as the $\alpha'$ band in the $PtCoO_2$ film. (g), (h), and (i) Corresponding measurements on the $PdCrO_2$ film, with the $\beta$ band representing the palladium bulk band, and the additional $\beta''$ band indicated by red diamonds in (i), which differs from the $\alpha'$ band and $\beta'$ band observed in the $PtCoO_2$ and $PdCoO_2$ film shown in (c) and (f), as indicated by the light yellow and red triangles in (i). The $PtCoO_2$ and $PdCoO_2$ film data were acquired at a temperature of 6 K, while the $PdCrO_2$ film data were obtained at 50 K.

band folding at the magnetic Brillouin zone boundary, we will show below that these new states in $PtCoO_2$ films reflect a new surface reconstruction. This observation is corroborated by the observation of the same $\alpha'$ bands identified in another $PtCoO_2$ film using 16.85 eV photons, whereas these bands were absent in the ARPES data obtained with 40.8 eV photon energy, as shown in Figs. S6 and S7 in the supplementary material. The absence might be related to the photon energy dependence of the relevant photoemission cross section.

In a palladium-terminated $PdCoO_2$ film, analogous new band features referred to as $\beta'$ bands were found as shown in Figs. 2(c) and 2(d). The $PdCoO_2$ bulk state, denoted as the $\beta$ band, primarily exhibits palladium character according to prior work on $PdCoO_2$ single crystals.[14,27,28] It is important to note that the $\beta'$ bands in the $PdCoO_2$ film differ from the symmetry of surface states attributed to palladium and $CoO_2$ layers, as discussed in previous work.[14,24,29] Thus, the presence of the $\alpha'$ bands in $PtCoO_2$ films and the $\beta'$ bands in $PdCoO_2$ films is new territory compared to prior work.

The band structure of the $PdCrO_2$ film is shown in Figs. 2(e) and 2(f). Although the band structures of $PdCoO_2$ and $PtCoO_2$ are similar, that of $PdCrO_2$ exhibits distinctive behavior. This band structure exhibits a hexagonal pocket $\beta$ band centered at Γ point, representing the primary palladium character of the bulk state, in line with previous reports on $PdCrO_2$ single crystals.[11,13] The bulk bands observed in $PtCoO_2$, $PdCoO_2$, and $PdCrO_2$ films are consistent with our independent DFT calculations (see Fig. S11 in

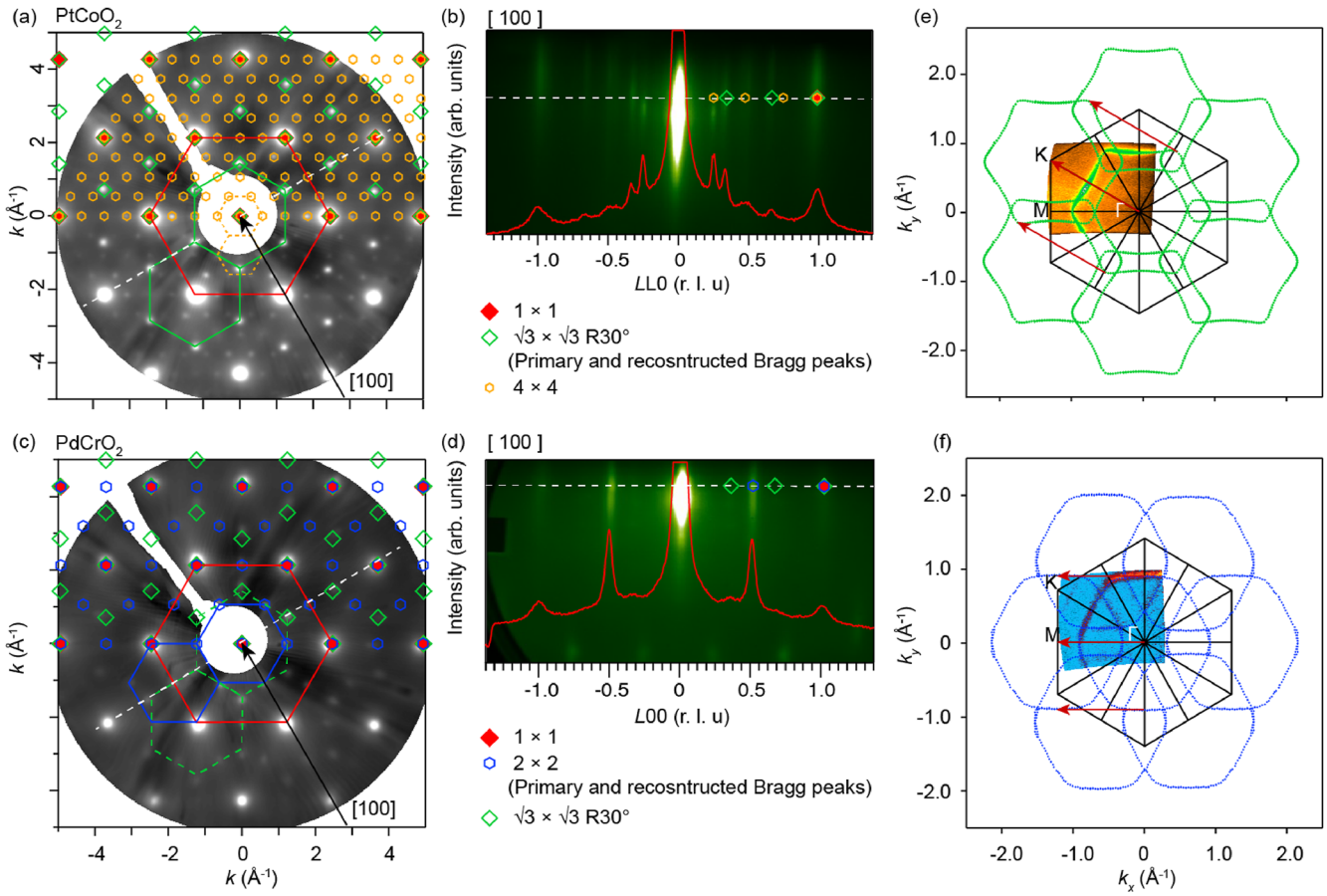


**FIG. 4.** Surface reconstructions observed via LEED, RHEED, and ARPES. (a) LEED image of the $PtCoO_2$ film, where red solid diamonds correspond to the 1 × 1 reciprocal lattice. The green diamonds highlight the $\sqrt{3} \times \sqrt{3}$ reconstruction, as shown in the hexagonal green zone. The yellow hexagons indicate the observed 4 × 4 reconstruction in LEED, signified by the zone covered by dashed yellow lines. The black arrow corresponds to the [100] electron-beam direction of the RHEED image shown in (b). The white dashed line denotes the direction along which the RHEED image is captured. (b) RHEED pattern of the $PtCoO_2$ in the (100)* reciprocal lattice plane, corresponding to the white dashed line in (a). The dashed line indicates where the intensity data are extracted. The symbols on the dashed line match those on the white dashed line in (a), precisely aligning with the peaks observed in the RHEED image. (c) and (d) The same information as (a) and (b), respectively, but for the $PdCrO_2$ film. In (c), the red solid diamonds correspond to the 1 × 1 reciprocal lattice of the $PdCrO_2$ film, while the blue hexagons illustrate the 2 × 2 reconstruction shown in the blue hexagonal zone. A weak $\sqrt{3} \times \sqrt{3}$ reconstruction is indicated by the green diamonds in the dashed hexagonal green zones. (e) The Fermi surface of the $PtCoO_2$ film, where the central hexagonal pocket made up of green dots is extracted from where the bulk state $\alpha$ band crosses $E_F$. The surrounding hexagonal pockets are multiplied by the $\sqrt{3} \times \sqrt{3}$ folding. The red arrows indicate one of the nesting directions. (f) The same as (e), but for the $PdCrO_2$ film with the 2 × 2 reconstruction.

the supplementary material).[28] Nonetheless, the $PdCrO_2$ film also presents additional band features, denoted as $\beta''$ bands, which have not been reported in any prior delafossite materials. Note that the data for the $\beta''$ band in our $PdCrO_2$ film were obtained above the AFM transition temperature, suggesting that this band's presence is not associated with the AFM order in $PdCrO_2$. Nevertheless, the $\beta''$ bands are also present in the ARPES result of this $PdCrO_2$ film taken at 6 K, as shown in the supplementary material (Fig. S5). Moreover, the $\beta''$ band exhibits distinct dispersion compared to the reconstructed bands driven by AFM order in $PdCrO_2$ single crystals. In addition, the $\beta''$ bands are also present in a thinner $PdCrO_2$ film (4 nm thickness) as shown in Fig. S8 in the supplementary material. Nonetheless, not all the $PdCrO_2$ films with $CrO_2$ termination exhibit the $\beta''$ bands. Figure S9 in the supplementary material shows the dispersions at the M point of the $PtCoO_2$ and $PdCrO_2$ films.

We further compare the dispersion of these additional bands in the metallic delafossite films along the Γ-K direction, as illustrated in Fig. 3. Figures 3(a), 3(d), and 3(g) display the momentum dispersion curves at $E_F$ of the $PtCoO_2$, $PdCoO_2$, and $PdCrO_2$ films, respectively. The high-intensity $\alpha$ band in Fig. 3(a) and the highly dispersive $\beta$ bands observed in Figs. 3(d) and 3(g) correspond to the platinum and palladium bulk state in $PtCoO_2$, $PdCoO_2$, and $PdCrO_2$ films, as previously shown in Figs. 2(a), 2(c), and 2(e). The $\alpha'$ band in the $PtCoO_2$ film and the $\beta'$ band in the $PdCoO_2$ film exhibit similar dispersion, as illustrated in Figs. 3(c) and 3(f). Conversely, the $\beta''$ band in the $PdCrO_2$ film displays a distinct $k_F$ position compared to the $\alpha'$ band in the $PtCoO_2$ film and the $\beta'$ band in the $PdCrO_2$ film, as shown in Fig. 3(i). In addition, Fig. 3(a) reveals the subtle presence of an additional $\gamma$ band in the $PtCoO_2$ film, a feature also shown in Fig. 2(a). This $\gamma$ band could potentially be associated with a platinum surface state, similar to the palladium surface state observed in $PdCoO_2$ single crystals.[14] Given the analogous behavior of the $\alpha'$ band in the $PtCoO_2$ film and the $\beta'$ band in the $PdCoO_2$ film, our analysis now focuses on the comparison between the $PtCoO_2$ and $PdCrO_2$ films.

To investigate the surface reconstructions of the $PtCoO_2$ film and the $PdCrO_2$ films, we analyzed their LEED images displayed in Figs. 4(a) and 4(c). In the composite LEED image of the $PtCoO_2$ film [Fig. 4(a)], the reciprocal lattice of $PtCoO_2$ is marked by red solid diamonds, as shown by the red solid hexagonal zone in the center. A distinct $\sqrt{3} \times \sqrt{3}$ reconstruction with a 30° rotation is indicated by the green diamonds along with a less pronounced $4 \times 4$ reconstruction signified by the yellow hexagons. The $\sqrt{3} \times \sqrt{3}$ reconstruction with a 30° rotation is simplistically denoted as $\sqrt{3} \times \sqrt{3}$. The green zones (solid lines) and yellow zones (dashed lines) denote the pronounced $\sqrt{3} \times \sqrt{3}$ and the subtle $4 \times 4$ reconstructed orientations, respectively. Importantly, these reconstruction patterns observed in the $PtCoO_2$ LEED image correspond precisely with those observed in the RHEED image along the [100] direction in reciprocal space, as evidenced by comparing the white dashed line in Fig. 4(a) with the peak positions in the RHEED image [Fig. 4(b)]. Similarly, the LEED image for the $PdCrO_2$ film [Fig. 4(c)] displays the reciprocal lattice of $PdCrO_2$ denoted by red solid diamonds, with a strong $2 \times 2$ reconstruction denoted by blue hexagons and a weak $\sqrt{3} \times \sqrt{3}$ reconstruction represented by green diamonds. The blue zones (solid lines) and green zones (dashed lines) represent the strong $2 \times 2$ and the weak $\sqrt{3} \times \sqrt{3}$ reconstructed orientations, respectively. Once again, the reconstructions identified in the LEED images are seen to be consistent with the peaks observed in the RHEED image along the [100] direction, as indicated in Figs. 4(c) and 4(d), ensuring a consistent interpretation of the surface reconstructions across different imaging techniques.

A detailed analysis of the Fermi surface measured on the $PtCoO_2$ film is performed by extracting the bulk $\alpha$ band at $E_F$ in Fig. 2(a) and folding it with the $\sqrt{3} \times \sqrt{3}$ reconstruction. The corresponding results are presented in Fig. 4(e), where we observed a striking match between the additional band features at $E_F$ ($\alpha'$ band) and the folded band with the $\sqrt{3} \times \sqrt{3}$ reconstruction. Despite its presence in both the LEED and RHEED analyses of the $PtCoO_2$ film, we did not observe any additional $4 \times 4$ reconstruction at $E_F$. It is worth noting that the intensity of the $4 \times 4$ reconstruction is considerably weaker compared to the $\sqrt{3} \times \sqrt{3}$ reconstruction, which may account for its limited visibility. Similarly, we folded the bulk band of the $PdCrO_2$ film at $E_F$, which revealed an almost exact correspondence between the additional $\beta'$ band and the band folded with the $2 \times 2$ reconstruction, as presented in Fig. 4(f). Interestingly, the band structure of the $PdCrO_2$ film at $E_F$ did not exhibit the $\sqrt{3} \times \sqrt{3}$ reconstruction suggested by the LEED result. This discrepancy could be attributed to the relatively weak $\sqrt{3} \times \sqrt{3}$ reconstruction compared to the $2 \times 2$ reconstruction, as evidenced in the LEED analysis of the $PdCrO_2$ film presented in Fig. 4(f).

Our findings provide conclusive evidence for the primary $\sqrt{3} \times \sqrt{3}$ surface reconstruction in the $PtCoO_2$ film, which is also observed in the $PdCoO_2$ film. In addition, the main $2 \times 2$ reconstruction has been firmly identified in the $PdCrO_2$ film. Evidence of these reconstructions is consistently detected by the ARPES, LEED, and RHEED measurements on our films. Nonetheless, such specific reconstructions have not been previously reported in delafossite materials, which are usually prepared by cleavage of single crystals, prompting further investigation into their origin. Figure 4 elucidates the consistency between the RHEED data and the reconstructions observed in LEED results. We further conduct a comparative analysis of the RHEED images of the $PdCoO_2$ film [in Figs. 2(c) and 2(d)] at various stages of growth, enabling real-time monitoring during the growth process. These RHEED images, presented in Fig. S10 in the supplementary material, reveal the emergence of one-third-order peaks during the annealing of the as-grown $PdCoO_2$ film in distilled ozone and persist throughout the cooling process. Remarkably, these one-third-order peaks in the $PdCoO_2$ film mirror those seen in the $PtCoO_2$ film [Fig. 4(b)], corresponding to the $\sqrt{3} \times \sqrt{3}$ reconstruction. This observation suggests a potential link between the $\sqrt{3} \times \sqrt{3}$ reconstruction and excess oxygen on the film surface, implying that excess oxygen on the surface may mitigate the polar surface charge by reducing the surface energy. Note that the $PdCoO_2$ film possesses a full layer of palladium termination, introducing a positive charge. The additional oxygen helps to neutralize this polar surface charge, thus lowering the surface energy. Addressing the challenges of polar surfaces can be approached in various ways; for instance, when the $PtCoO_2$ film is grown by co-deposition, the result is a mixed termination by platinum and $CoO_2$. It is important to mention that all films are subjected to annealing in distilled ozone to provide fresh surfaces prior to the ARPES measurement; thus, there are multiple steps during growth and annealing where

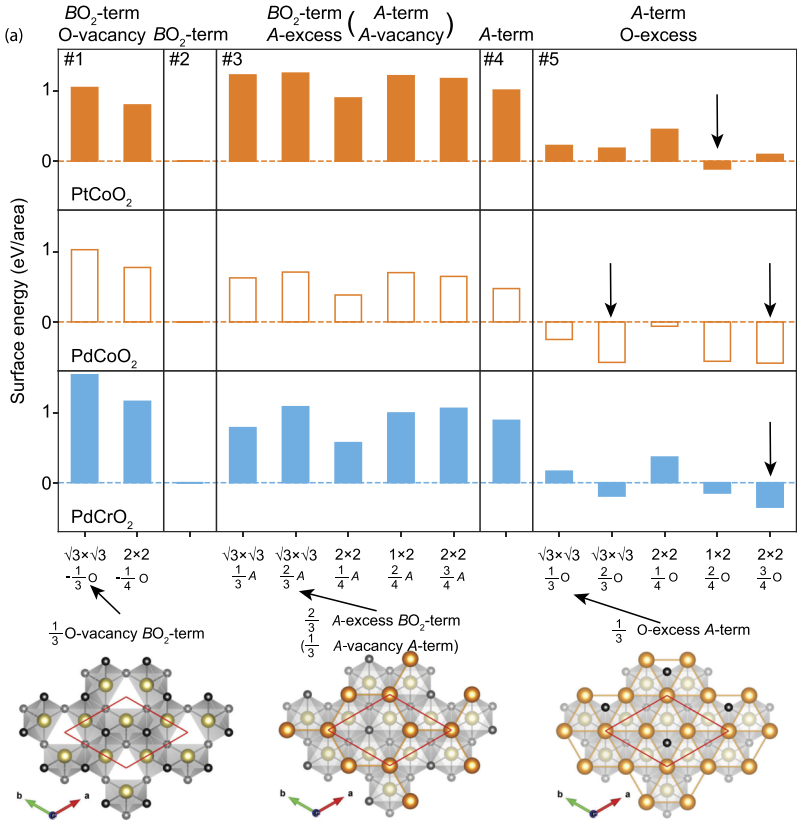


**FIG. 5.** Surface energy analysis via first-principles DFT calculations for $PtCoO_2$, $PdCoO_2$, and $PdCrO_2$. The surface energies for different scenarios are compared against the $BO_2$ terminated surface in panel 2, i.e., oxygen vacancy, *A* excess, and oxygen excess, which modify the pristine *A* or $BO_2$ terminated surfaces and lead to $\sqrt{3} \times \sqrt{3}$ and $2 \times 2$ reconstruction. The vertical arrows point to the surface configurations with the lowest surface energy. "$BO_2$-term" stands for films terminated by a $CoO_2$ layer or $CrO_2$ layer, and "*A*-term" represents films terminated by a palladium or platinum layer. We used non-spin-polarized calculations for $PtCoO_2$ and $PdCoO_2$, and spin-polarized calculations for $PdCrO_2$, assuming a ferromagnetic configuration.

excess oxygen is supplied and could, thus, attach to the film surface should it be energetically favorable to do so.

Given the limitations of STEM to clearly resolve surface atoms, we next discuss the potential surface scenarios compatible with $\sqrt{3} \times \sqrt{3}$ and $2 \times 2$ reconstructions through DFT calculations. We have chosen to omit scenarios leading to the weak $4 \times 4$ reconstruction observed in $PtCoO_2$ due to the complexity introduced by their large supercell sizes. For the $\sqrt{3} \times \sqrt{3}$ reconstruction, the scenarios considered include the presence of one oxygen vacancy ($\sqrt{3} \times \sqrt{3}$ −1/3 oxygen), an excess of *A*-site atoms on a $BO_2$-terminated surface ($\sqrt{3} \times \sqrt{3}$ + $n$/3 *A*-site), and an excess of oxygen atoms on an *A*-terminated surface ($\sqrt{3} \times \sqrt{3}$ + $n$/3 oxygen), where $n$ equals 1 or 2. Similarly, for the $2 \times 2$ reconstruction, we explore the possibility of one oxygen vacancy ($2 \times 2$ − 1/4 oxygen), an excess of *A* atoms on the $BO_2$-terminated surface ($2 \times 2$ + $n$/4 *A*-site), and an excess of oxygen atoms on an *A*-terminated surface ($2 \times 2$ + $n$/4 oxygen), where $n$ is 1, 2, or 3. In addition, we have calculated the pristine surfaces, denoted as $BO_2$- and *A*-site termination in Fig. 5. For each scenario, we search for the lowest energy surface atomic configuration and then calculate its surface energy relative to the pristine $BO_2$-terminated surface. The results are illustrated in Fig. 5, with computational details available in the supplementary material (Fig. S12).

For all three compounds studied, the surface energies associated with creating an oxygen vacancy or adding excess *A*-site atom(s) on $BO_2$-terminated surfaces are found to be positive, often exceeding 0.5 eV per unit cell area (panels 1 and 3 in Fig. 5). This indicates that both removing oxygen from and adding *A* atom(s) onto the $BO_2$-terminated surface are energetically costly processes. Conversely, the introduction of excess oxygen atoms on *A*-terminated surfaces significantly lowers the surface energy, as shown in panel 5 in Fig. 5. In certain cases, this adjustment leads to negative surface energies when compared to the $BO_2$-terminated surface, suggesting that adding oxygen to *A*-terminated surfaces is energetically favorable and could lead to more stable surface configurations.

The above results further support the hypothesis that the reconstructions observed in $PtCoO_2$ (mixed termination) and $PdCoO_2$ (palladium termination) films could be attributed to excess oxygen, which effectively reduces the surface energy. In our ARPES and LEED results, the $\sqrt{3} \times \sqrt{3}$ reconstruction is manifest on both

$PtCoO_2$ and $PdCoO_2$ films. Nonetheless, our calculations indicate that scenarios leading to the $\sqrt{3} \times \sqrt{3}$ reconstruction do not consistently exhibit the lowest surface energy. This discrepancy might originate from the limitation of DFT in accurately determining surface energies or could be due to additional complexities present on the experimental film surfaces that are not fully accounted for in the DFT models. For instance, the mixed termination observed in $PtCoO_2$ could alter the energy landscape in ways not captured by our DFT simulations. Therefore, while our DFT calculations align with our ARPES and LEED findings in suggesting that excess oxygen contributes to the observed reconstructions, they do not conclusively determine the size of the reconstructed supercell. In the case of $PdCrO_2$ films grown with $CrO_2$ terminations, scenarios involving excess oxygen are not applicable. This leaves the $2 \times 2$ reconstruction with 1/4 *A*-site addition as a scenario with relatively low surface energy, aligning with our experimental observations and presenting a possible explanation for the surface structure of $PdCrO_2$ films.

In conclusion, we have successfully synthesized high-quality $PtCoO_2$, $PdCoO_2$, and $PdCrO_2$ films by MBE, followed by a comprehensive investigation of their surface reconstructions using a combination of ARPES, LEED, and RHEED. Our investigations have unveiled the presence of surface reconstructions in these films, including a $\sqrt{3} \times \sqrt{3}$ reconstruction in $PtCoO_2$ films with mixed platinum–$CoO_2$ terminations and in palladium-terminated $PdCoO_2$ film, as well as a distinctive $2 \times 2$ reconstruction is seen in $CrO_2$-terminated $PdCrO_2$ films. These findings, which are corroborated by ARPES, LEED, and RHEED analyses, highlight surface reconstructions in these films that have not been previously reported in delafossite single crystals. These new reconstructions are likely closely linked to the polar terminations of the as-grown thin films, where the additional atoms on pristine surfaces could potentially lower their surface energy. DFT calculations shed light on the relative instability of surfaces terminated with *A* (*A* = Pt, Pd) atoms compared to those terminated with $BO_2$ (*B* = Co, Cr), as evidenced by their higher formation energies. Nonetheless, the presence of excess oxygen can significantly mitigate these energies, leading to reconstructed configurations. Our results show general consistency (with some discrepancies) between the calculated and experimentally observed sizes of the reconstructed supercells. By elucidating the distinct surface reconstructions from the surface states associated with different terminations in metallic delafossites, as well as from the electronic reconstructions driven by magnetic order, our work not only contributes to the understanding of surface phenomena in delafossite materials but also sets the stage for further exploration of highly two-dimensional studies in this intriguing class of materials.

See the supplementary material for a description of how the $PtCoO_2$ and $PdCrO_2$ films are grown and analyzed, additional characterization by TEM, RHEED, and ARPES, and details on the method of DFT calculations.

This paper was primarily supported by the U.S. Department of Energy, Office of Basic Sciences, Division of Materials Science and Engineering under Award No. DE-SC0002334. This research was funded in part by the Gordon and Betty Moore Foundation's EPiQS Initiative (Grant Nos. GBMF3850 and GBMF9073 to Cornell University). This paper made use of the Cornell Center for Materials Research shared facilities, which are supported through the NSF Materials Research Science and Engineering Centers Program (Grant No. DMR-1719875). B.D.F., M.R.B., and B.P. acknowledged support from the National Science Foundation Platform for the Accelerated Realization, Analysis, and Discovery of Interface Materials (PARADIM) under Cooperative Agreement No. DMR-2039380. This paper also made use of the Cornell Energy Systems Institute Shared Facilities partly sponsored by the NSF (Grant No. MRI DMR-1338010) and the Kavli Institute at Cornell. Substrate preparation was performed, in part, at the Cornell NanoScale Facility, a member of the National Nanotechnology Coordinated Infrastructure, which is supported by the NSF (Grant No. NNCI-2025233). P.K. acknowledged support from the European Research Council (through the QUESTDO Project, 714193) and The Leverhulme Trust (Grant No. RPG-2023-256).

## AUTHOR DECLARATIONS

### Conflict of Interest

The authors have no conflicts to disclose.

### Author Contributions

**Qi Song**: Conceptualization (equal); Data curation (equal); Formal analysis (equal); Writing – original draft (equal). **Zhiren He**: Formal analysis (equal); Methodology (equal); Writing – review & editing (supporting). **Brendan D. Faeth**: Data curation (equal); Formal analysis (equal); Writing – review & editing (equal). **Christopher T. Parzyck**: Data curation (equal); Formal analysis (supporting); Writing – review & editing (equal). **Anna Scheid**: Data curation (equal); Formal analysis (equal). **Chad J. Mowers**: Data curation (supporting); Writing – review & editing (supporting). **Yufan Feng**: Data curation (supporting). **Qing Xu**: Data curation (equal); Formal analysis (equal). **Sonia Hasko**: Data curation (supporting). **Jisung Park**: Resources (supporting). **Matthew R. Barone**: Resources (supporting). **Y. Eren Suyolcu**: Data curation (equal). **Peter A. van Aken**: Resources (supporting). **Betül Pamuk**: Formal analysis (supporting); Writing – review & editing (supporting). **Craig J. Fennie**: Resources (supporting). **Phil D. C. King**: Investigation (equal); Writing – review & editing (supporting). **Kyle M. Shen**: Resources (supporting). **Darrell G. Schlom**: Funding acquisition (equal); Investigation (equal); Resources (equal); Supervision (equal); Writing – review & editing (equal).

## DATA AVAILABILITY

Datasets generated and analyzed during the course of this study are available at https://doi.org/10.34863/0ngf-h790.

## REFERENCES

[1] C. W. Hicks, A. S. Gibbs, A. P. Mackenzie, H. Takatsu, Y. Maeno, and E. A. Yelland, "Quantum oscillations and high carrier mobility in the delafossite $PdCoO_2$," Phys. Rev. Lett. **109**, 116401 (2012).

[2] P. Kushwaha, V. Sunko, P. J. Moll, L. Bawden, J. M. Riley, N. Nandi, H. Rosner, M. P. Schmidt, F. Arnold, E. Hassinger, T. K. Kim, M. Hoesch, A. P. MacKenzie, and P. D. C. King, "Nearly free electrons in a 5*d* delafossite oxide metal," Sci. Adv. **1**, e1500692 (2015).

[3]A. P. Mackenzie, "The properties of ultrapure delafossite metals," Rep. Prog. Phys. **80**, 032501 (2017).
[4]V. Eyert, R. Frésard, and A. Maignan, "On the metallic conductivity of the delafossites $PdCoO_2$ and $PtCoO_2$," Chem. Mater. **20**, 2370–2373 (2008).
[5]K. Kim, H. C. Choi, and B. I. Min, "Fermi surface and surface electronic structure of delafossite $PdCoO_2$," Phys. Rev. B **80**, 035116 (2009).
[6]K. P. Ong, D. J. Singh, and P. Wu, "Unusual transport and strongly anisotropic thermopower in $PtCoO_2$ and $PdCoO_2$," Phys. Rev. Lett. **104**, 176601 (2010).
[7]Y. Zhang, F. Tutt, G. N. Evans, P. Sharma, G. Haugstad, B. Kaiser, J. Ramberger, S. Bayliff, Y. Tao, M. Manno, J. Garcia-Barriocanal, V. Chaturvedi, R. M. Fernandes, T. Birol, W. E. Seyfried, Jr., and C. Leighton, "Crystal-chemical origins of the ultrahigh conductivity of metallic delafossites," Nat. Commun. **15**, 1399 (2024).
[8]S. Kumar, C. Multunas, B. Defay, D. Gall, and R. Sundararaman, "Ultralow electron-surface scattering in nanoscale metals leveraging Fermi-surface anisotropy," Phys. Rev. Mater. **6**, 085002 (2022).
[9]H. Takatsu, H. Yoshizawa, and Y. Maeno, "Comparative study of conductive delafossites with and without frustrated spins on a triangular lattice, $PdMO_2$ ($M$ = Cr; Co)," J. Phys.: Conf. Ser. **145**, 012046 (2009).
[10]H. Takatsu and Y. Maeno, "Single crystal growth of the metallic triangular-lattice antiferromagnet $PdCrO_2$," J. Cryst. Growth **312**, 3461–3465 (2010).
[11]H. J. Noh, J. Jeong, B. Chang, D. Jeong, H. S. Moon, E. J. Cho, J. M. Ok, J. S. Kim, K. Kim, B. I. Min, H. K. Lee, J. Y. Kim, B. G. Park, H. D. Kim, and S. Lee, "Direct observation of localized spin antiferromagnetic transition in $PdCrO_2$ by angle-resolved photoemission spectroscopy," Sci. Rep. **4**, 3680 (2014).
[12]M. D. Le, S. Jeon, A. I. Kolesnikov, D. J. Voneshen, A. S. Gibbs, J. S. Kim, J. Jeong, H. J. Noh, C. Park, J. Yu, T. G. Perring, and J. G. Park, "Magnetic interactions in $PdCrO_2$ and their effects on its magnetic structure," Phys. Rev. B **98**, 024429 (2018).
[13]V. Sunko, F. Mazzola, S. Kitamura, S. Khim, P. Kushwaha, O. J. Clark, M. D. Watson, I. Marković, D. Biswas, L. Pourovskii, T. K. Kim, T. L. Lee, P. K. Thakur, H. Rosner, A. Georges, R. Moessner, T. Oka, A. P. Mackenzie, and P. D. King, "Probing spin correlations using angle-resolved photoemission in a coupled metallic/Mott insulator system," Sci. Adv. **6**, eaaz0611 (2020).
[14]F. Mazzola, V. Sunko, S. Khim, H. Rosner, P. Kushwaha, O. J. Clark, L. Bawden, I. Marković, T. K. Kim, M. Hoesch, A. P. Mackenzie, and P. D. C. King, "Itinerant ferromagnetism of the Pd-terminated polar surface of $PdCoO_2$," Proc. Natl. Acad. Sci. U. S. A. **115**, 12956–12960 (2018).
[15]V. Sunko, H. Rosner, P. Kushwaha, S. Khim, F. Mazzola, L. Bawden, O. J. Clark, J. M. Riley, D. Kasinathan, M. W. Haverkort, T. K. Kim, M. Hoesch, J. Fujii, I. Vobornik, A. P. Mackenzie, and P. D. C. King, "Maximal Rashba-like spin splitting via kinetic-energy-coupled inversion-symmetry breaking," Nature **549**, 492–496 (2017).
[16]F. Mazzola, C. M. Yim, V. Sunko, S. Khim, P. Kushwaha, O. J. Clark, L. Bawden, I. Marković, D. Chakraborti, T. K. Kim, M. Hoesch, A. P. Mackenzie, P. Wahl, and P. D. King, "Tuneable electron–magnon coupling of ferromagnetic surface states in $PdCoO_2$," npj Quantum Mater. **7**, 20 (2022).
[17]P. F. Carcia, R. D. Shannon, P. E. Bierstedt, and R. B. Flippen, "$O_2$ electrocatalysis on thin film metallic oxide electrodes with the delafossite structure," J. Electrochem. Soc. **127**, 1974–1978 (1980).
[18]T. Harada, K. Fujiwara, and A. Tsukazaki, "Highly conductive $PdCoO_2$ ultrathin films for transparent electrodes," APL Mater. **6**, 046107 (2018).
[19]P. Yordanov, W. Sigle, P. Kaya, M. E. Gruner, R. Pentcheva, B. Keimer, and H.-U. Habermeier, "Large thermopower anisotropy in $PdCoO_2$ thin films," Phys. Rev. Mater. **3**, 085403 (2019).
[20]M. Brahlek, G. Rimal, J. M. Ok, D. Mukherjee, A. R. Mazza, Q. Lu, H. N. Lee, T. Z. Ward, R. R. Unocic, G. Eres, and S. Oh, "Growth of metallic delafossite $PdCoO_2$ by molecular beam epitaxy," Phys. Rev. Mater. **3**, 093401 (2019).
[21]J. M. Ok, M. Brahlek, W. S. Choi, K. M. Roccapriore, M. F. Chisholm, S. Kim, C. Sohn, E. Skoropata, S. Yoon, J. S. Kim, and H. N. Lee, "Pulsed-laser epitaxy of metallic delafossite $PdCrO_2$ films," APL Mater. **8**, 051104 (2020).
[22]J. Sun, M. R. Barone, C. S. Chang, M. E. Holtz, H. Paik, J. Schubert, D. A. Muller, and D. G. Schlom, "Growth of $PdCoO_2$ by ozone-assisted molecular-beam epitaxy," APL Mater. **7**, 121112 (2019).
[23]T. Harada, K. Sugawara, K. Fujiwara, M. Kitamura, S. Ito, T. Nojima, K. Horiba, H. Kumigashira, T. Takahashi, T. Sato, and A. Tsukazaki, "Anomalous Hall effect at the spontaneously electron-doped polar surface of $PdCoO_2$ ultrathin films," Phys. Rev. Res. **2**, 013282 (2020).
[24]Q. Song, J. Sun, C. T. Parzyck, L. Miao, Q. Xu, F. V. E. Hensling, M. R. Barone, C. Hu, J. Kim, B. D. Faeth, H. Paik, P. D. C. King, K. M. Shen, and D. G. Schlom, "Growth of $PdCoO_2$ films with controlled termination by molecular-beam epitaxy and determination of their electronic structure by angle-resolved photoemission spectroscopy," APL Mater. **10**, 091113 (2022).
[25]R. Wei, P. Gong, M. Zhao, H. Tong, X. Tang, L. Hu, J. Yang, W. Song, X. Zhu, and Y. Sun, "Solution-processable epitaxial metallic delafossite oxide films," Adv. Funct. Mater. **30**, 2002375 (2020).
[26]Y. Tarn, M. Sinha, C. Pasco, D. G. Schlom, T. M. McQueen, K. M. Shen, and B. D. Faeth, "An algorithm for subtraction of doublet emission lines in angle-resolved photoemission spectroscopy," J. Electron Spectrosc. Relat. Phenom. **265**, 147323 (2023).
[27]H.-J. Noh, J. Jeong, J. Jeong, E.-J. Cho, S. B. Kim, K. Kim, B. I. Min, and H.-D. Kim, "Anisotropic electric conductivity of delafossite $PdCoO_2$ studied by angle-resolved photoemission spectroscopy," Phys. Rev. Lett. **102**, 256404 (2009).
[28]V. Sunko, *Angle Resolved Photoemission Spectroscopy of Delafossite Metals*, 1st ed. (Springer, Cham, 2019).
[29]T. Harada, "Thin-film growth and application prospects of metallic delafossites," Mater. Today Adv. **11**, 100146 (2021).

# Supplementary material for "Surface reconstructions and electronic structure of metallic delafossite thin films"

Qi Song,[1] Zhiren He,[2] Brendan D. Faeth,[3] Christopher T. Parzyck,[4] Anna Scheid,[5] Chad J. Mowers,[4] Yufan Feng,[6,7] Qing Xu,[6] Sonia Hasko,[6] Jisung Park,[1] Matthew R. Barone,[6] Y. Eren Suyolcu,[5] Peter A. van Aken,[5] Betül Pamuk,[6,8] Craig J. Fennie,[2] Phil D. C. King,[9] Kyle M. Shen,[4,10] and Darrell G. Schlom[1,10,11]

[1)]*Department of Materials Sciences and Engineering, Cornell University, Ithaca, New York 14853, USA*

[2)]*Department of Applied and Engineering Physics, Cornell University, Ithaca, New York 14853, USA*

[3)]*Platform for the Accelerated Realization, Analysis, and Discovery of Interface Materials (PARADIM), Cornell University, Ithaca, New York 14853, USA*

[4)]*Department of Physics, Laboratory of Atomic and Solid State Physics, Cornell University, Ithaca, New York 14853, USA*

[5)]*Max Planck Institute for Solid State Research, Heisenbergstrasse 1, Stuttgart 70569, Germany*

[6)]*Platform for the Accelerated Realization, Analysis, and Discovery of Interface Materials (PARADIM), Cornell University, Ithaca, New York 14853, USA*

[7)]*Robert Frederick Smith School of Chemical and Biomolecular Engineering, Cornell University, Ithaca, New York 14853, USA*

[8)]*Department of Physics, Williams College, Williamstown, Massachusetts 01267, USA*

[9)]*SUPA, School of Physics and Astronomy, University of St Andrews, St Andrews KY16 9SS, UK*

[10)]*Kavli Institute at Cornell for Nanoscale Science, Ithaca, New York 14853, USA*

[11)]*Leibniz-Institut für Kristallzüchtung, Max-Born-Straße 2, 12489 Berlin, Germany*

(*Electronic mail: schlom@cornell.edu)

(*Electronic mail: qisong@cornell.edu)

## A. Film growth

$PtCoO_2$, $PdCoO_2$, and $PdCrO_2$ films were all grown on (001) sapphire substrates, which had been annealed to 1000 °C for 6 hours prior to film growths. During the deposition, distilled ozone (a mixture of approximately 80% ozone and 20% oxygen) was introduced at a background partial pressure of $5 \times 10^{-6}$ to $8.5 \times 10^{-6}$ Torr during all of the growths. The fluxes of platinum, palladium, cobalt, and chromium, evaporated from MBE effusion cells, were adjusted to achieve a flux of approximately $1 \times 10^{13}$ atoms $cm^2s^{-1}$, as determined by a quartz crystal microbalance. This initial flux calibration was further refined by measuring the thickness of a platinum calibration film grown on a (111) $(ZrO_2)_{0.905}(Y_2O_3)_{0.09}$ substrate by x-ray reflectivity (XRR);[1] the same was done for palladium. The $Co_3O_4$ calibration film was grown on a (100) $MgAl_2O_4$ substrate and measured by XRR; the $Cr_2O_3$ calibration film was grown on a (001) sapphire substrate and measured by XRR.[1]

For the $PtCoO_2$ film growth, the substrates were heated to temperatures ranging from 500 °C to 540 °C, as monitored by an optical pyrometer operating at a wavelength of 980 nm. To obtain single-phase epitaxial $PtCoO_2$ films, it was crucial to use an epitaxial $PdCoO_2$ film as a buffer layer on a (001) $Al_2O_3$ substrate, which promoted the nucleation and epitaxial overgrowth of the $PtCoO_2$ film. For all of the films in this study, a four or seven formula-unit-thick buffer layer of $PdCoO_2$ on the (001) $Al_2O_3$ substrates was employed. Subsequent codeposition of platinum, cobalt, and ozone was carried out under conditions where the excess platinum supplied would desorb as PtO (g), following a similar concept of the absorption-controlled growth conditions utilized for the growth of $PdCoO_2$.[2]. The ratio of Pt:Co in this codeposited flux ranged from 1.3 to 1.4. Additional details of $PdCoO_2$ growth are described in the supplementary material of Ref. 2.

For the $PdCrO_2$ growth, the substrates were heated to around 600 °C. A 12-nm-thick $CuCrO_2$ film is employed as a buffer layer to stabilize the delafossite structure of $PdCrO_2$ under a background pressure of $1 \times 10^{-6}$ Torr of distilled ozone. With a continuous flux of distilled ozone giving rise to a background pressure of $5 \times 10^{-6}$ Torr, platinum and chromium shutters were actuated to supply monolayer doses of platinum and chromium following the sequence of atomic layers along the *c*-axis of the crystal structure of $PdCrO_2$. The first seven formula-unite-thick layers of $PdCrO_2$ are grown with a Pd:Cr ratio of 1:1. After the deposition of seven formula-unit-thick layers, 20% excess palladium is supplied in each shuttered dose, i.e., a Pd:Cr ratio of 1.2:1. The excess palladium supplied in each shuttered dose is to make up for the evaporation of palladium

oxide at the relatively high substrate temperature and ozone pressure used, similar to the growth of $PdCoO_2$ films by a shutter-controlled method.[2]

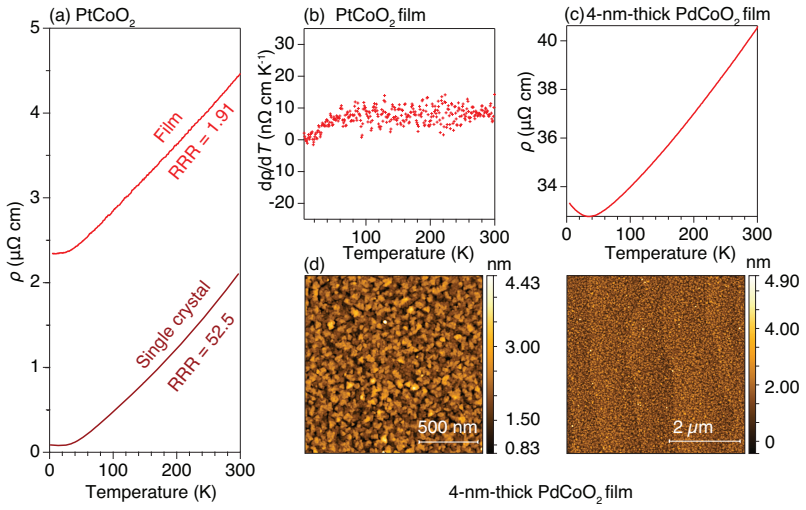


FIG. S1: (a) Resistivity comparison between the 13.3 nm $PtCoO_2$ film (after subtraction of the contribution from the 4-nm-thick $PdCoO_2$ buffer layer) and a $PtCoO_2$ single crystal (from Ref. 3). Due to the rough surface of the $PtCoO_2$ shown in Fig. 1(c), the approximate resistivity of the $PtCoO_2$ film is what is plotted in (a). The residual resistivity ratio (RRR = $\rho_{300K}/\rho_{4K}$) of the single crystal is from Ref. 4. (b) Derivative of the film resistivity with respect to temperature as a function of the temperature for the same $PtCoO_2$ film, presenting linear temperature dependence at high temperatures. The calculation used a Savitzky-Golay smooth filter.[5] (c) Temperature-dependent resistivity measurements of a 4.0-nm-thick $PdCoO_2$ film. (d) Atomic force microscopy images of the $PdCoO_2$ film characterized in (c). The resistance subtraction to estimate the resistance of the $PtCoO_2$ film ($R_{PtCoO2}$) from which the resistivity of the $PdCoO_2$ film shown in Fig. 1(e) is calculated involved the following formula: $\frac{1}{R_{Total}} = \frac{t_{PtCoO2}}{R_{PtCoO2}} + \frac{1}{R_{PdCoO2}}$, where $t_{PtCoO2}$ is the average thickness of the $PtCoO_2$ film and $R_{Total}$ is the resistance measured for the $PtCoO_2$/$PdCoO_2$ bilayer.

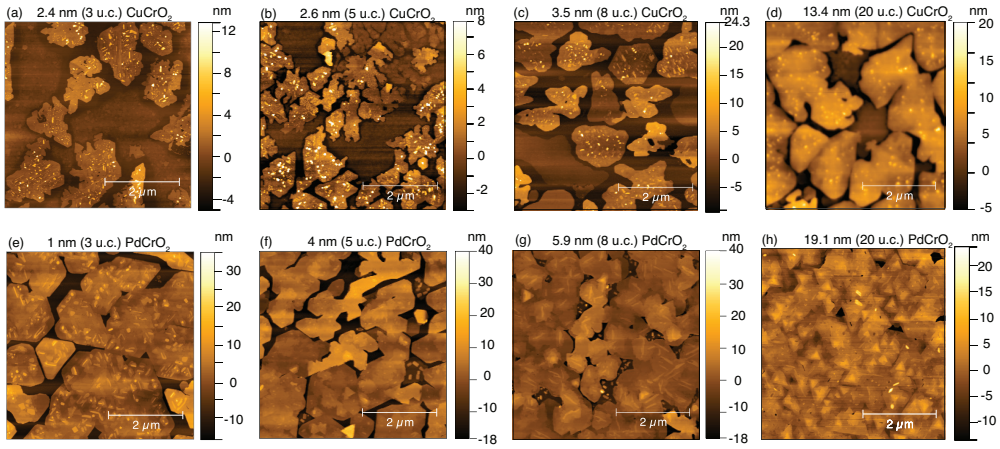


FIG. S2: Atomic force microscopy images of (a)-(d) varying thicknesses of $CuCrO_2$ films and (e)-(h) varying thicknesses of $PdCrO_2$ films grown on top of 12-nm-thick $CuCrO_2$ films. Due to island growth, the ultra-thin $CuCrO_2$ films do not cover the entire substrate; similarly, the ultra-thin $PdCrO_2$ films also exhibit island growth on and between the underlying $CuCrO_2$ islands. The thickness given refers to the average thickness of the films.

## B. Scanning transmission electron microscopy (STEM) investigations

STEM investigations were carried out using a JEOL JEM-ARM200F equipped with a cold field-emission gun and a probe Cs-corrector (DCOR, CEOS GmbH). Measurements were performed at ambient temperatures with an acceleration voltage of 200 kV. Electron energy-loss spectroscopy (EELS) acquisition was performed using a Gatan GIF Quantum ERS imaging filter with an entrance aperture of 5 mm, camera length of 1.5 cm, and probe semi-convergence angle of 20.4 mrad, resulting in a collection semi-angle of 111 mrad.

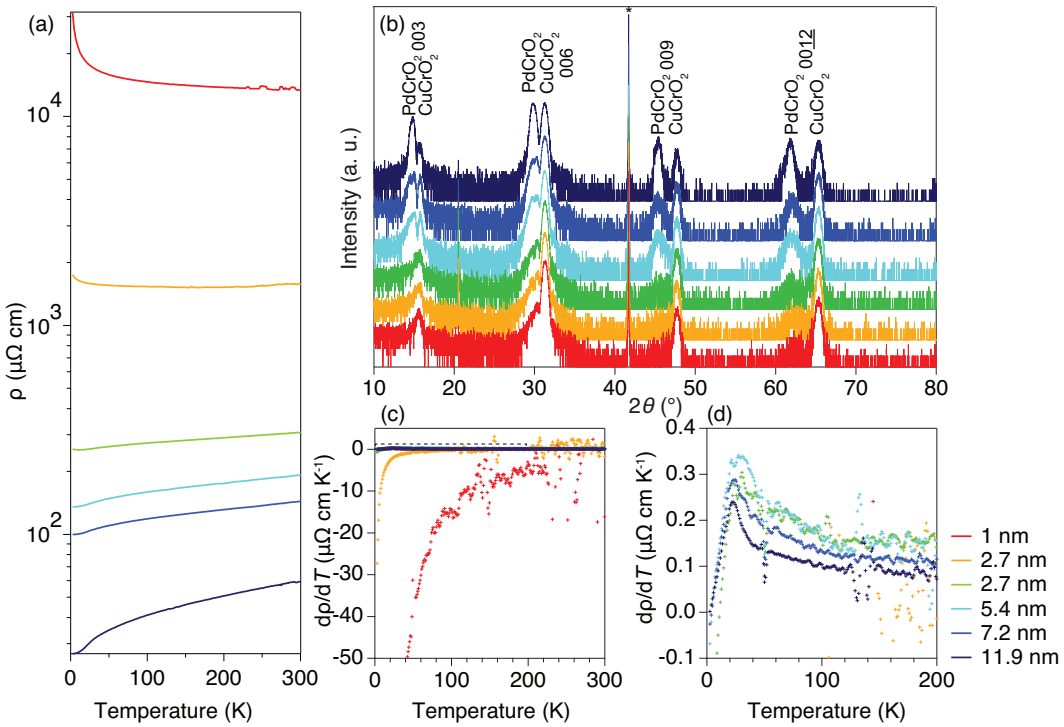


FIG. S3: Structural and electrical characterization of $PdCrO_2$ thin films grown on 12-nm-thick (average thickness) $CuCrO_2$ buffer layers on (001) $Al_2O_3$ substrates by MBE. (a) Temperature-dependent resistivity measurements of the $PdCrO_2/CuCrO_2$ bilayer films with varying (average) thickness of the $PdCrO_2$ film. The resistivities plotted ignore the effect of the $CuCrO_2$ buffer layer as the in-plane resistivity ( $\rho_{11}$) of (001) $CuCrO_2$ is over 7 orders of magnitude higher than $\rho_{11}$ of $PdCrO_2$ at room temperature and this ratio grows larger as the temperature is lowered because $CuCrO_2$ is a semiconductor whereas $PdCrO_2$ is a metal.[6,7] Similar to $PdCoO_2$ films,[8] the ultra-thin $PdCrO_2$ films show insulating behavior. Note due to island growth, electrical percolation influences the electrical transport properties. Among the films with an average thickness of 2.7 nm, one (in yellow color) shows insulating behavior, while another (in green color) shows metallic behavior. (b) $\theta$-$2\theta$ X-ray diffraction scans of the same $PdCrO_2$ thin films characterized in (a). * denotes the 006 peak of the (001) $Al_2O_3$ substrate. The intensity of $PdCrO_2$ peaks increases with the thickness of the $PdCrO_2$ films as it should. (c) Derivative of the film resistivity with respect to temperature as a function of temperature for the same $PdCrO_2$ thin films in (a). The calculation used a Savitzky-Golay smooth filter.[5] (d) Close-up of the dashed rectangle in (c). The thicker films that exhibit metallic behavior show a peak in the $d\rho/dT$ at low temperatures, similar to that observed in $PdCrO_2$ single crystals driven by AFM order. The peak locations vary from 22 K to 26 K, differing from the $T_N$ = 37 K in $PdCrO_2$ single crystals.

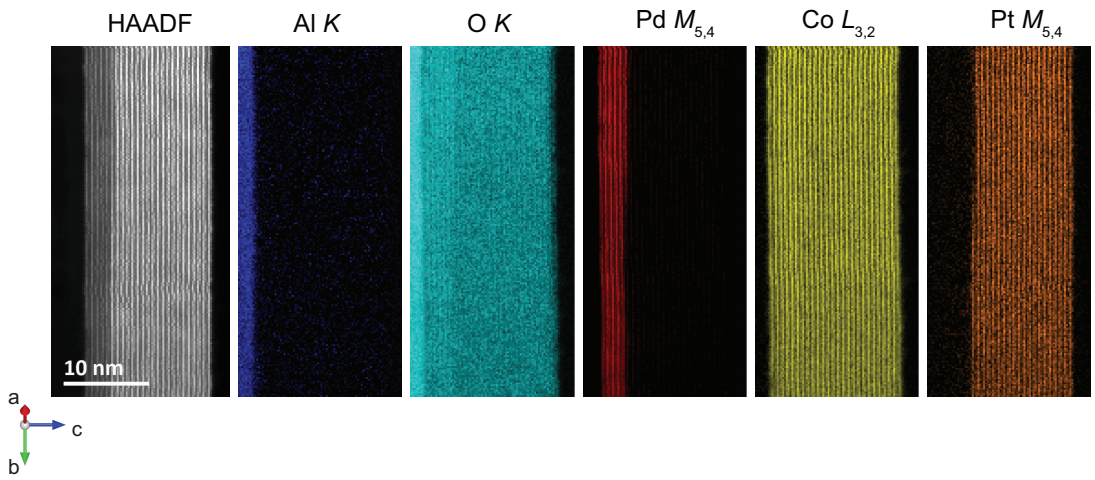


FIG. S4: EELS elemental mapping confirms a homogeneous elemental distribution in the alternating $Pd^{+}$ and $CoO_2^{-}$ with sharp interfaces between substrate, buffer layer, and thin film.

## C. Electronic structure

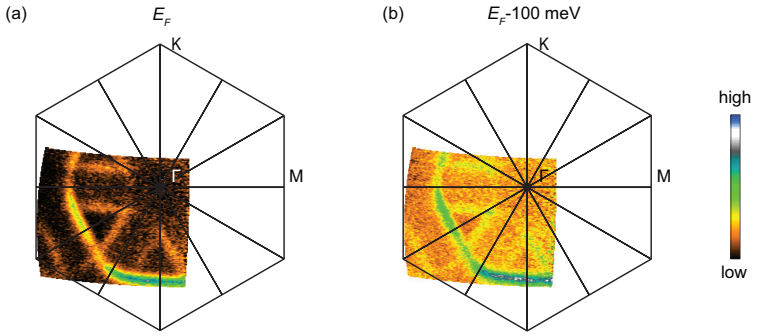


FIG. S5: Photoemission intensity maps of the $PdCrO_2$ film shown in Fig. 2 collected using 21.2 eV photons at 6 K. The same $2 \times 2$ reconstruction in the $PdCrO_2$ film is also present below $T_N$. Note the AFM-driven $\sqrt{3} \times \sqrt{3}$ reconstruction seen in $PdCrO_2$ single crystals is absent at the Fermi surface of the $PdCrO_2$ film, which might be related to the lower photon energy used in our ARPES measurements.

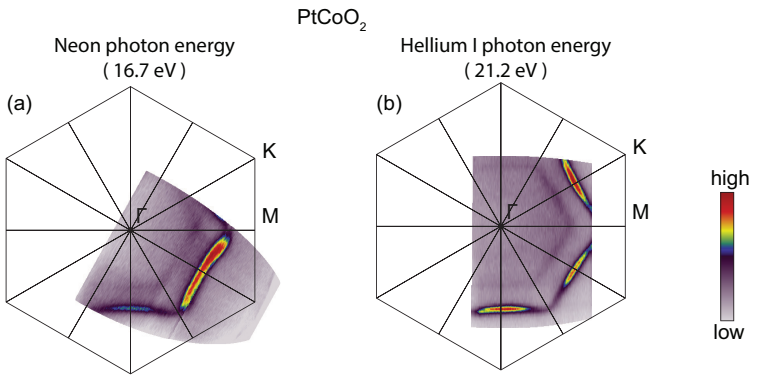


FIG. S6: Photoemission intensity maps of a $PtCoO_2$ film at photon energies of (a) 16.7 eV and (b) 21.2 eV, respectively, revealing the presence of the $\sqrt{3} \times \sqrt{3}$ reconstruction at both photon energies.

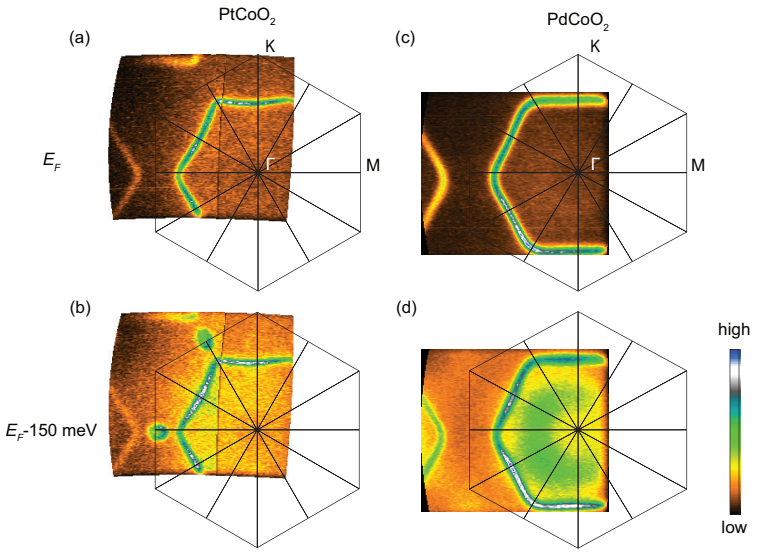


FIG. S7: Photoemission intensity maps of $PtCoO_2$ and $PdCoO_2$ films were obtained using a photon energy of 40.4 eV (Helium II). At this energy, the reconstructed bands are not visible. A comparison experiment was conducted by initially measuring the ARPES using a 40.4 eV photon energy and subsequently with a 21.2 eV photon energy. Interestingly, the reconstruction is only observed in the data acquired using the 21.2 eV and 16.7 eV photon energies, as shown in Fig. S6. This energy dependence in the reconstruction bands could potentially be attributed to the relevant photoemission cross section.

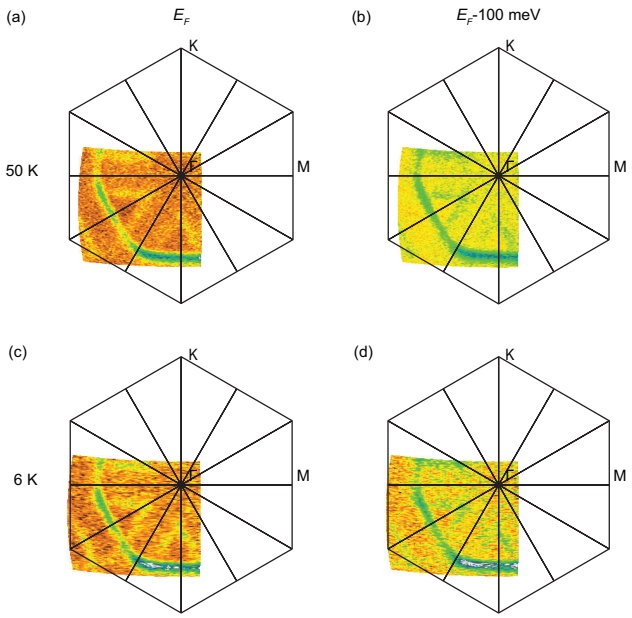


FIG. S8: Photoemission intensity maps of a 4-nm-thick $PdCrO_2$ film obtained using a photon energy of 21.2 eV. The $2 \times 2$ reconstruction feature is present both below and above $T_N$.

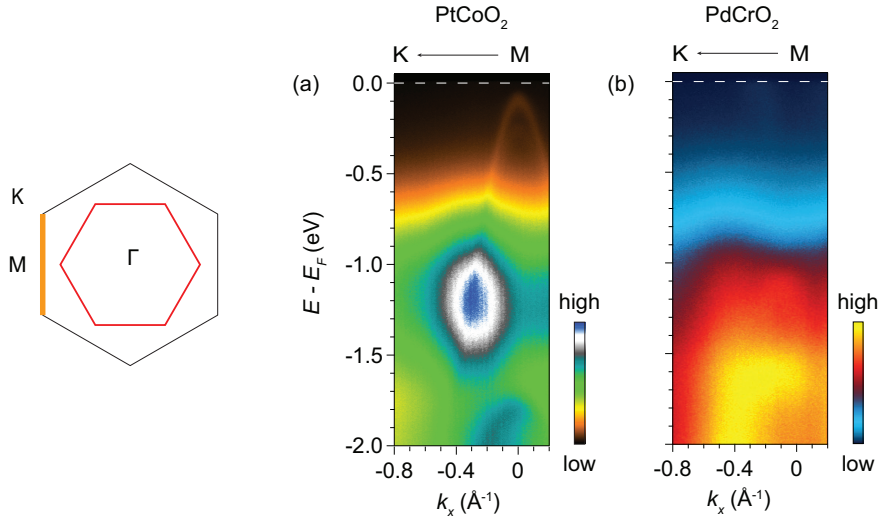


FIG. S9: Photoemission intensity distributions along the K-M-K direction of $PtCoO_2$ and $PdCrO_2$ films obtained using a photon energy of 21.2 eV.

## D. Oxygen excess on the surface during growth

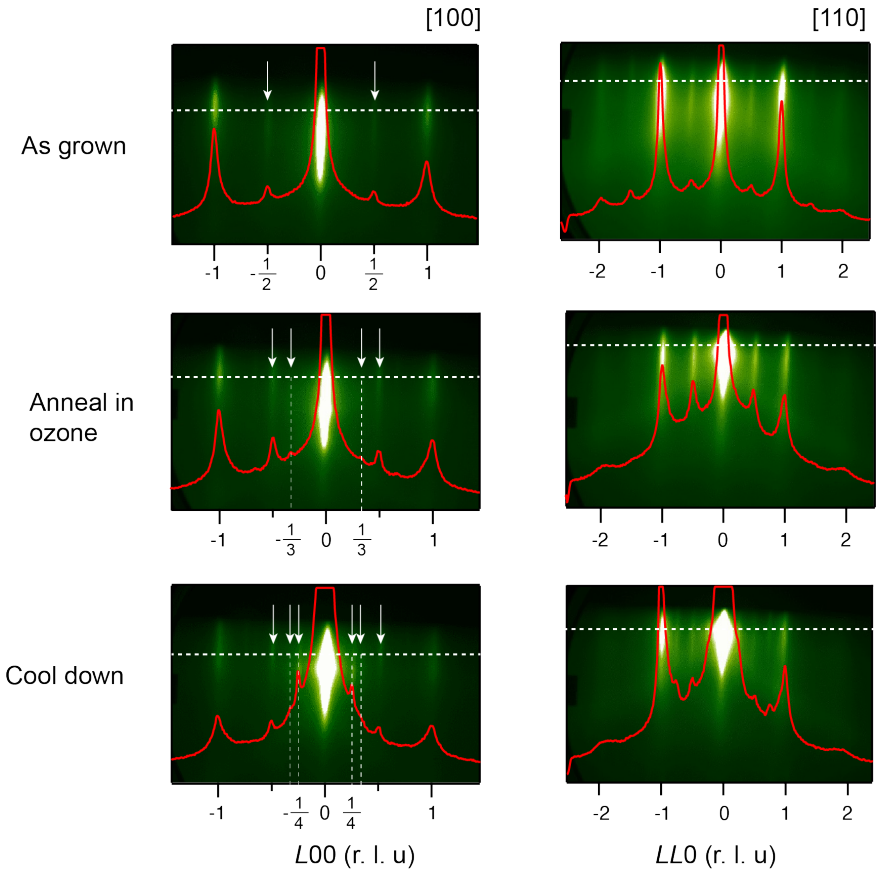


FIG. S10: RHEED patterns of the $PdCoO_2$ film captured along the [100] and [110] azimuths during the growth process. In the as-grown film at $T_{sub} \approx 580$ °C, prominent main-order peaks and half-order peaks are visible. Upon annealing in ozone, faint one-third-order peaks emerge. During the subsequent cool-down to room temperature, strong quarter-order peaks show up, persisting alongside the one-third-order peaks. Note in some ARPES measurements of other $PdCoO_2$ films lacking the presence of one-third-order peaks in RHEED, the reconstructed band is not observed.[2]

## E. DFT

First-principles calculations were performed using the Vienna Ab initio Simulation Package (VASP) with PBEsol exchange-correlation functional and projector augmented-wave pseudopotentials. We applied a kinetic energy cutoff of 520 eV and a $k$-mesh of $12 \times 12 \times 2$ for the bulk conventional cell. We employed the method of Methfessel-Paxton of order 1 to describe the partial occupancy at $E_F$, with a smearing value of 0.1 eV.

Symmetric slabs were used for band structure and Fermi surface calculations, see Figs. S12(a)

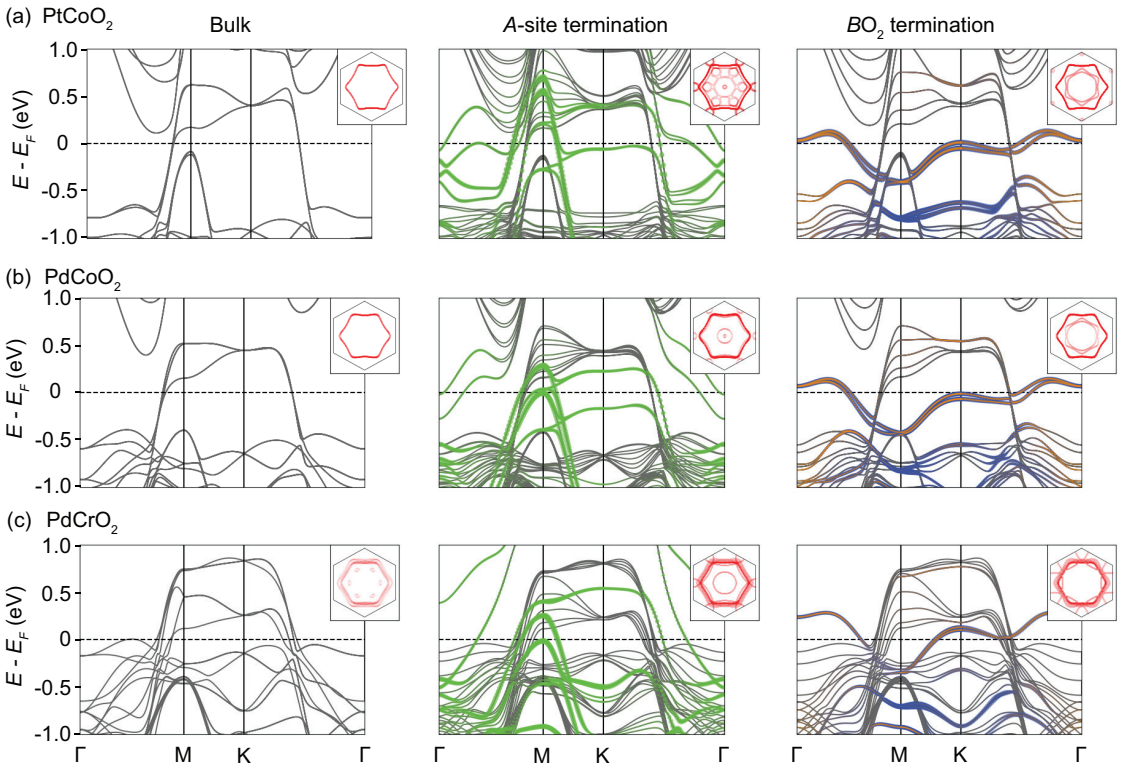


FIG. S11: Band-structure calculations were performed for $PtCoO_2$, $PdCoO_2$, and $PdCrO_2$ with different terminations. Inserts are the corresponding Fermi surfaces. The green, blue, and orange dots highlight the projection onto the surface *A*-site, *B*-site, and O atoms, respectively, which were obtained from DFT using the post-processing tool VASPKIT.[9].

and S12(b). At least 20 Å of vacuum along the *c* direction separated the periodic images. The atoms near the top and bottom surface were relaxed, followed by non-self-consistent calculations to compute the band structure and Fermi surface. Spin-orbit coupling was included. For $ACoO_2$ (*A* = Pd, Pt) the bulk systems relax to a nonmagnetic state, in agreement with experimental observations. Experimentally, the ground states of $PdCrO_2$ are antiferromagnetic below the Néel temperature and paramagnetic above the transition temperature. The 120° antiferromagnetic order requires a $\sqrt{3} \times \sqrt{3}$ reconstruction while we observe a $2 \times 2$ reconstruction in our ARPES measurements, which are above the Néel temperature. To correctly simulate the systems with chromium, magnetic order needs to be imposed. Therefore, we have assumed a ferromagnetic order along the *c* direction for $PdCrO_2$. The electronic structure shows the changes due to surface termination qualitatively but does not aim to reproduce the paramagnetic phase above the Néel temperature in our experiment and may not accurately capture the correlation effect in the $CrO_2$

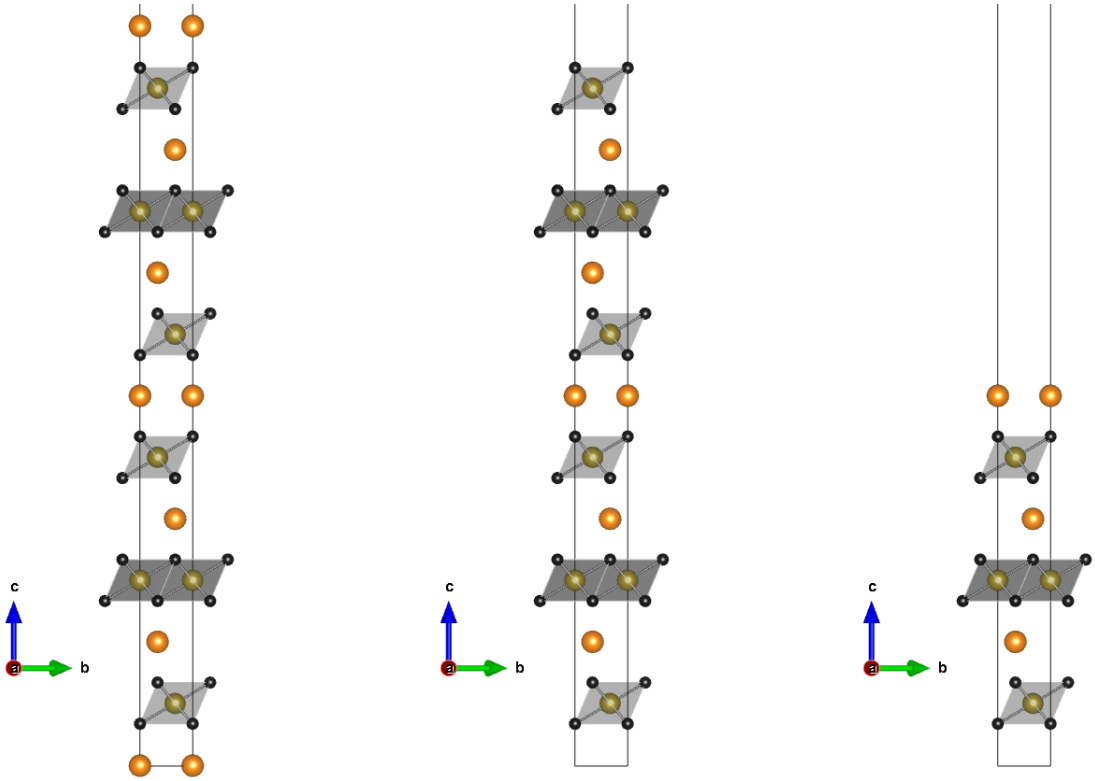


(a) (b) (c)

FIG. S12: Symmetric slabs with (a) $A$-termination (b) $BO_2$-termination used in the band structure and Fermi surface calculations. Atoms near the top and bottom surfaces are relaxed. (c) An example of the asymmetric slab with $A$-termination at the top surface is used in the surface energy calculation. The bottom is $BO_2$-terminated, and the top surface varies with different surface scenarios. Only the top atoms are relaxed.

layer. A more detailed study for bulk $PdCrO_2$ can be found in Ref. 10. A comparison between bulk and surface terminated bands shows similarity between the three compounds, i.e., additional bands crossing the Fermi level arising from surface atoms.

We also calculate the surface magnetization for the $A$-site terminated surfaces. The ground state of the $A$-site terminated surfaces are ferromagnetic with a small magnetization on the surface $A$ atom 0.4 $\mu$B, in agreement with the experiments.[11] The surface 120° AFM state is 20 meV per u.c. area higher in energy than the surface ferromagnetic ground state – showing that the effect of surface magnetization is small compared to the surface energy differences between different vacancy scenarios. Therefore, for the calculation of surface energy, we used non-spin-polarized calculations for $PtCoO_2$ and $PdCoO_2$, and spin-polarized calculations for $PdCrO_2$, assuming a fer-

romagnetic configuration. The results for the three compounds were tested against results obtained from spin-polarized calculations with Hubbard U = 4 eV, and no qualitative changes were found, confirming a small effect of magnetic configuration on the structural properties and surface energy for $PdCrO_2$.

The relative surface formation energy $E_{\Delta\text{surf}}$ was computed by

$$E_{\Delta\text{surf}} = E_{\text{surf}} - E_{\text{ref}} \pm N \times \mu_{\text{atom}}, \tag{S1}$$

where $E_{\text{surf}}$ is the energy of the $\sqrt{3} \times \sqrt{3}$ or $2 \times 2$ reconstructed surface. $E_{\text{ref}}$ is the energy of the reference structure, and here we chose the clean $BO_2$-terminated surface as our reference, since here only the relative energies of the configurations matter. $N \times \mu_{\text{atom}}$ is the chemical potential of the $N$ atoms added or removed from the reference structure. The chemical potential for Pt/Pd was estimated from the DFT energy of bcc Pt/Pd metal. For oxygen, we used half the DFT energy of a single $O_2$ molecule in a large box. The results are

$$\mu_{\text{O}} = -4.688, \quad \mu_{\text{Pt}} = -6.965, \quad \mu_{\text{Pd}} = -5.692$$

in units of eV.

To reduce the computational cost, we applied an asymmetric slab to compute $E_{\text{surf}}$ and $E_{\text{ref}}$, as illustrated in Fig. S12(c). We employed $BO_2$-terminated bottom and various surface terminations with different reconstructions. Only atoms near the top surface were relaxed. A dipole correction was applied to eliminate the energy due to the artificial electric field resulting from the asymmetric slab[12]. In addition, we extrapolated the surface energy to infinite vacuum width to eliminate the interactions between periodic images. For the situation with $A$-excess on a $BO_2$-termination or oxygen excess on the $A$-termination, the original locations of excess $A$ site or oxygen atoms with vertical $A$-O bonds tend not to have the lowest energy. Therefore, for each situation, we compared the energies of all potential surface binding sites for an excess of $A$ site or oxygen after surface relaxation to determine the ground state structure and energy.

## REFERENCES


[1]J. Sun, C. T. Parzyck, J. H. Lee, C. M. Brooks, L. F. Kourkoutis, X. Ke, R. Misra, J. Schubert, F. V. Hensling, M. R. Barone, Z. Wang, M. E. Holtz, N. J. Schreiber, Q. Song, H. Paik, T. Heeg, D. A. Muller, K. M. Shen, and D. G. Schlom, "Canonical approach to cation flux calibration in oxide molecular-beam epitaxy," Phys. Rev. Mater. **6**, 033802 (2022).

[2]Q. Song, J. Sun, C. T. Parzyck, L. Miao, Q. Xu, F. V. E. Hensling, M. R. Barone, C. Hu, J. Kim, B. D. Faeth, H. Paik, P. D. C. King, K. M. Shen, and D. G. Schlom, "Growth of $PdCoO_2$ films with controlled termination by molecular-beam epitaxy and determination of their electronic structure by angle-resolved photoemission spectroscopy," APL Mater. **10**, 091113 (2022).

[3]N. Nandi, T. Scaffidi, P. Kushwaha, S. Khim, M. E. Barber, V. Sunko, F. Mazzola, P. D. C. King, H. Rosner, P. J. W. Moll, M. König, J. E. Moore, S. Hartnoll, and A. P. Mackenzie, "Unconventional magneto-transport in ultrapure $PdCoO_2$ and $PtCoO_2$," npj Quantum Mater. **3**, 66 (2018).

[4]A. P. Mackenzie, "The properties of ultrapure delafossite metals," Rep. Prog. Phys. **80**, 032501 (2017).

[5]A. Savitzky and M. J. Golay, "Smoothing and Differentiation of Data by Simplified Least Squares Procedures," Anal. Chem. **36**, 1627–1639 (1964).

[6]M. Poienar, V. Hardy, B. Kundys, K. Singh, A. Maignan, F. Damay, and C. Martin, "Revisiting the properties of delafossite $CuCrO_2$: A single crystal study," J. Solid State Chem. **185**, 56–61 (2012).

[7]C. W. Hicks, A. S. Gibbs, A. P. Mackenzie, H. Takatsu, Y. Maeno, and E. A. Yelland, "Quantum Oscillations and High Carrier Mobility in the Delafossite $PdCoO_2$," Phys. Rev. Lett. **109**, 116401 (2012).

[8]J. Sun, M. R. Barone, C. S. Chang, M. E. Holtz, H. Paik, J. Schubert, D. A. Muller, and D. G. Schlom, "Growth of $PdCoO_2$ by ozone-assisted molecular-beam epitaxy," APL Mater. **7**, 121112 (2019).

[9]V. Wang, N. Xu, J.-C. Liu, G. Tang, and W.-T. Geng, "Vaspkit: A user-friendly interface facilitating high-throughput computing and analysis using vasp code," Comput. Phys. Commun. **267**, 108033 (2021).

[10]F. Lechermann, "From basic properties to the Mott design of correlated delafossites," npj Comput. Mater. **7**, 120 (2021).

[11]F. Mazzola, V. Sunko, S. Khim, H. Rosner, P. Kushwaha, O. J. Clark, L. Bawden, I. Marković, T. K. Kim, M. Hoesch, A. P. Mackenzie, and P. D. C. King, "Itinerant ferromagnetism of the Pd-terminated polar surface of $PdCoO_2$," PNAS **115**, 12956–12960 (2018).

[12]J. Neugebauer and M. Scheffler, "Adsorbate-substrate and adsorbate-adsorbate interactions of Na and K adlayers on Al(111)," Phys. Rev. B **46**, 16067 (1992).